



HAL
open science

Visual metering of the urban radiative environment through 4π imagery

Jairo Acuña Paz y Miño, Claire Lawrence, Benoit Beckers

► To cite this version:

Jairo Acuña Paz y Miño, Claire Lawrence, Benoit Beckers. Visual metering of the urban radiative environment through 4π imagery. *Infrared Physics and Technology*, 2020, 110, pp.103463 -. 10.1016/j.infrared.2020.103463 . hal-03491609

HAL Id: hal-03491609

<https://hal.science/hal-03491609>

Submitted on 5 Sep 2022

HAL is a multi-disciplinary open access archive for the deposit and dissemination of scientific research documents, whether they are published or not. The documents may come from teaching and research institutions in France or abroad, or from public or private research centers.

L'archive ouverte pluridisciplinaire **HAL**, est destinée au dépôt et à la diffusion de documents scientifiques de niveau recherche, publiés ou non, émanant des établissements d'enseignement et de recherche français ou étrangers, des laboratoires publics ou privés.



Distributed under a Creative Commons Attribution - NonCommercial 4.0 International License

Visual metering of the Urban Radiative Environment through 4π imagery

Jairo Acuña Paz y Miño, Claire Lawrence and Benoit Beckers

Urban Physics Joint Laboratory, E2S UPPA, Université de Pau et des Pays de l'Adour, Anglet, France

E-mail: j.acuna@univ-pau.fr

Abstract

In urban climate or thermal comfort, radiative exchanges are often expressed in terms of Mean Radiant Temperature. Considering that a single temperature does not properly represent the radiative environment, an alternative method is proposed here to observe it in depth. This method is giving an alternative for evaluating the urban radiant environment through a measurement that covers a solid angle of 4π steradians.

The results are validated by comparison with those obtained by the black-globe method. The difference is always less than two degrees.

This paper proposes the joint use of photographic and LWIR thermal cameras for a radiometric study. Due to the nature of its approach, this method allows for spectral discrimination, in two bands: 380 nm - 780 nm and 7.5 μm to 13 μm . This encourages the separate analysis of each part of the spectrum as well as the ensemble.

Furthermore, the small duration of each measurement opens up the possibility of studying the radiative environment free from disturbances due to the inertia of the measuring device.

Keywords: Urban physics, Imagery, Radiative Exchange, Mean Radiant Temperature

1. Introduction

Scientists and practitioners from a broad range of disciplines including urbanism [Ren 2011], urban physics [Beckers 2013], climatology [Eliasson 1996], geography [Grimmonds 2002], and biometeorology [Lindberg 2018] undertake the study of radiative exchanges in the urban scene. Historically, these studies are framed in two ways of approaching the radiative environment. The first concerns the Urban Heat Island (UHI), which is caused in part by an increase of factors like: solar absorption, longwave radiation from the sky and the storage of sensible heat; and a decrease in factors such as: net longwave radiation loss, evapotranspiration and total turbulent heat loss [Oke 1982]. The second one leans towards outdoor thermal comfort seeking to evaluate thermal stress. For this purpose, indicators as the Physiologically Equivalent Temperature (PET) [Höppe 1999] or the Universal Thermal Climate Index (UTCI) [Fiala 2012] are used, both of them account for the radiant environment.

Today, climate change increases the thermal load in urban areas, accentuating the effects of UHI as predicted by [Voogt 2002]. These rising temperatures in the city not only

significantly affect outdoor thermal comfort [Oke 1987, Givoni 1998, Pearlmutter 2006, Chen 2012], but they may also cause a great impact on the energy consumption of buildings [Santamouris 2001].

This has led research into methods that act mainly on the radiative environment. Some of them aim to mitigate the UHI from the outdoor thermal comfort, based on the assumption that modifying the scene's microclimate has an impact on the city also at a larger scale [Santamouris 2014, Takebayashi 2007, Akbari 2016].

This renewed interest in radiative exchanges in the city requires more refined measurements that represent the real complexity of the scene under investigation.

The *Mean Radiant Temperature*, MRT or T_{mrt} , is the most widely used meteorological parameter, as it characterizes the effect of the radiant environment on thermal comfort [Fanger 1972]. T_{mrt} is defined as the "uniform surface temperature of an enclosure in which an occupant would exchange the same amount of radiation as in the actual non-uniform enclosure" [ASHRAE, 2001]. Although this indicator is conceptually simple, measuring it entails several constraints [Kántor 2011] and loses the link to urban

geometry that is important from a designer's point of view [Givoni 1998, Nikolopoulou 2007].

One of the most widespread ways of measuring T_{mrt} is with a black-globe thermometer. Introduced by Vernon in 1930, it is considered as the first and simplest "passive" radiometer. However, its response is affected by another factor: the convection [Bedford 1934]. Therefore, it is difficult to quantify radiation in rapidly changing conditions. As it is an integral radiation measurement, it combines the effect of the whole spectrum. Hence, it requires modifications to take into account the effects of shortwave and longwave radiation on non-black bodies [Thorsson 2007], and the shape of the thermometer limits the exploitation of its results since extrapolating them to other geometries is problematic.

Some research has been done seeking to address some of these issues to take the study further. [Richards, 1951; Koch, 1961; Gagge, 1967] excluded the influence of the wind by using radiometers. [Asano 1996; Tamura 2001] focused on displaying the longwave component using an IR scanner. [Thorsson 2007; Lindberg 2008] performed separate measurements for the two parts of the spectrum (shortwave and longwave) and accounted for the distribution of the radiant fluxes on non-spherical objects by combining measurements in six different directions and weighting values.

The 4π method is based on a previous work [Acuña Paz y Miño 2019] that explored the use of thermography to represent, in a synthetic way, the apparent temperature in different points along an urban promenade.

In this article, the shortwave contribution is included, which allows for the estimation of the Mean Radiant Temperature (T_{mrt}). The spatialized result of the method allows evaluating the influence that each surface of the scene has on the T_{mrt} , opening the door to a better understanding of the energy behavior of the city.

The 4π method is presented as an alternative for evaluating the radiant environment in a complex scene with rapidly changing conditions. In contrast to the black-globe thermometer, this imaging method uses radiance sensors thereby bypassing the influence of convection. To account for the spectral discrimination, shortwave and longwave radiation are measured separately, the first by *High Dynamic Range* (HDR) photography and the second by thermography.

2. General concepts

2.1 Radiometric Imagery

Thermal and photographic cameras measure the radiance of a scene, each in a different spectrum band since attenuation is strongly dependent on wavelength. Imagers have spectral ranges of measurement, which include the visible ($\sim 0.4\text{--}0.7\ \mu\text{m}$), shortwave infrared (SWIR $\sim 1\text{--}2\ \mu\text{m}$),

midwave infrared (MWIR $\sim 3\text{--}5\ \mu\text{m}$), and longwave infrared (LWIR $\sim 8\text{--}14\ \mu\text{m}$).

Although the atmosphere is essentially transparent for the visible range, for the infrared it is necessary to measure through the "atmospheric windows" (Figure 1). Since the study focuses on the temperatures of the scene, a LWIR thermal camera is used.

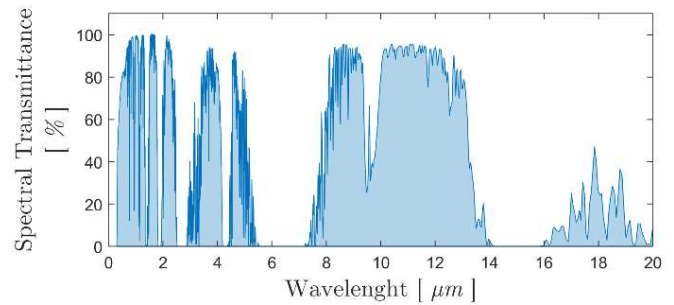


Figure 1. Atmospheric transmittance [Berk 1989]

These devices have optical and electronic components capable of detecting and measuring electromagnetic energy (radiant energy) which is later displayed in colors (tristimulus values) and temperatures.

This visualization of radiant energy provides an easy understanding of the scene because colors and temperatures are linked to perception. Nevertheless, they are the consequence of a post-processing based on hypotheses assumed by the operator during the setup of the device before the capture. Some parameters are emissivity, distance, white balance, and exposure time.

The magnitude studied through imaging radiometry is radiance. This is defined as the radiant flux of an emitter with a surface area that passes through a surface normal to the emission direction. Since this surface defines a solid angle in this direction, radiance is a true measure of the amount of radiation that is emitted, reflected, or transmitted into a certain direction and solid angle.

Analyzing radiance offers some advantages. Due to sensor linearity, measured response is linear with incident energy (radiance) while the temperature is non-linear. Besides, radiometric comparison between different objects tends to have less uncertainty since fewer assumptions are taken, and converting it to effective black body temperature is simple.

Planck's law states that any object can emit radiation at all wavelengths. However, it does not do so evenly across the spectrum.

For this study, radiative exchanges involve mainly two black bodies, the sun, and the earth (Figure 2).

The sun at 5778 K emits mainly in shortwave ($\lambda < 4\ \mu\text{m}$) and it peaks at 500 nm near the center of the visible spectrum. The mean temperature of the earth is 288 K. It, therefore, emits in longwave ($\lambda > 4\ \mu\text{m}$) and the maximum of radiation from a black body at this temperature occurs at

about 10 μm , approaching the center of the LWIR thermal camera's range, which goes from 7.5 μm to 13 μm .

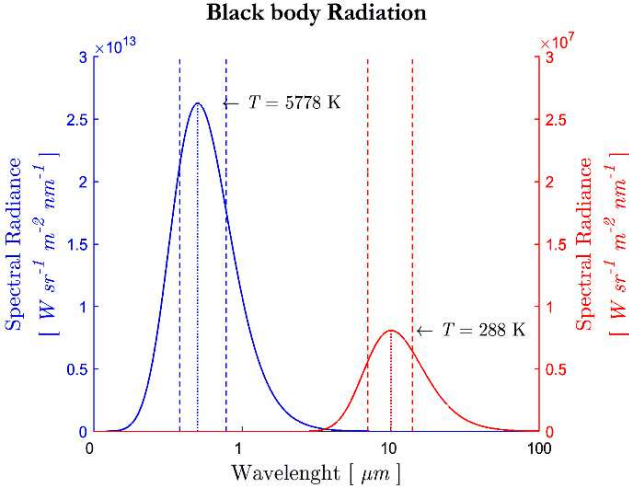


Figure 2. Spectral range measured by photography (blue) and by thermography (red): 380 nm - 780 nm and 7.5 μm to 13 μm

For any black body, the area under the curve (integrating Planck's law) corresponds to the radiance, L_e [$\text{W m}^{-2} \text{sr}^{-1}$] over the entire spectrum (between 0 and ∞). It is given by the following equation, where, $c = 299\,792\,458 \text{ m s}^{-1}$ is the speed of light in vacuum, $h = 6.626176 \times 10^{-34} \text{ W}\cdot\text{s}^2$ is the Planck's constant, and $k = 1.380662 \times 10^{-23} \text{ W s K}^{-1}$ is the Boltzmann's constant.

$$L_e = \int_0^{\infty} \frac{2hc^2}{\lambda^5} \frac{1}{e^{hc/\lambda kT} - 1} d\lambda \quad (1)$$

For a black body, radiance L and exitance M are linked:

$$L(T) = \frac{M(T)}{\pi} \quad (2)$$

The relationship between the radiance and the exitance of a black body at a given temperature corresponds to Stefan-Boltzmann's law. Solving the integral of equation (1) and considering equation (2), the exitance is expressed as follows:

$$M = \left(\frac{2\pi^5 k^4}{15h^3 c^2} \right) T^4 \quad (3)$$

2.2 The Mean Radiant Temperature

The T_{mrt} describes the effect of a discretized complex radiant environment taking into account both diffuse and direct shortwave irradiance (E_{sw} , I) [W m^{-2}] as well as longwave irradiance (E_{Lw}) [W m^{-2}] for each element (n), always considering the view factors (F_i , f_p). Note that the

absorption coefficient α may be different in each part of the spectrum.

$$\phi_r = \alpha_{Lw} \sum_{i=1}^n F_i E_{Lw} + \alpha_{sw} \sum_{i=1}^n F_i E_{sw} + \alpha_{sw} f_p I \quad (4)$$

Based on the flux resulting from the addition of the two irradiances, T_{mrt} [K] is calculated by the Stefan-Boltzmann law, where $\sigma = 5.670374419 \times 10^{-8} \text{ W m}^{-2} \text{ K}^{-4}$.

$$T_{mrt} = \sqrt[4]{\frac{\phi_r}{\sigma}} \quad (5)$$

2.3 The black-globe thermometer

In 1934, Bedford and Warner proposed a correction to quantify the radiative flux independently of the influence of the wind [Bedford 1934]. Since then, the black-globe thermometer is considered a reliable instrument that allows a simple evaluation of the radiative environment based on the concept of Mean Radiant Temperature.

At the equilibrium, the value of the temperature measured at the center of the globe is the result of heat exchanges by radiation and convection. The globe temperature (T_g) therefore represents a weighted average of the Mean Radiant Temperature (T_{mrt}) and the air temperature (T_{air}). This is the principle on which the measurement of T_{mrt} by the black-globe is grounded. T_g approaches T_{mrt} when the wind speed is low, whereas the higher the wind speed, the closer the value of T_g is to T_{air} . Consequently, in the presence of strong wind, the temperature measured is only that of the air.

These convective heat exchanges can be lessened by using a larger globe, but it considerably increases the response time. For a standard 0.15 m black-globe, this time could be between 20 and 30 minutes.

To calculate T_{mrt} based on the globe temperature, the following equation [De Dear 1988] is used:

$$T_{mrt} = T_g + \frac{h_{c_g}}{\varepsilon D_g^{0.4}} (T_g - T_{air}) \quad (6)$$

Where T_g [K] is the globe temperature, T_{air} [K] is the air temperature, ε is the emissivity of the black-globe, D_g is the adimensional diameter (actual diameter divided by the reference unit diameter of 1 m) and h_{c_g} an adimensional convection coefficient. In forced convection, h_{c_g} may be estimated taking into account the adimensional wind speed v_a (actual wind speed divided by the reference unit speed of 1 m/s).

$$h_{c_g} = 1.1 \times 10^8 v_a^{0.6} \quad (7)$$

This method raises two main issues. The difficulty of carrying measurements under changing conditions and the limited frequency with which these can be carried out, due to the inertia of the device. In addition, under windy conditions, the globe only records the air temperature and therefore the correction of the equation (6) has no effect.

The complexity of the radiative environment cannot be captured in the measurements because this method integrates the shortwave (diffuse, direct and reflected) and longwave contributions (the sky and the earth's surfaces) in every direction, hindering the analysis of the spatial distribution of the radiative environment as well as its effect on otherwise shaped bodies.

3. Material and methods

3.1 Material setup

The following hardware is used for the 4π method: a FLIR T460 thermal camera equipped with a FLIR T197412 wide-angle lens and a Canon PowerShot SX40 HS camera running a Canon Hack Development Kit (CHDK) to ensure absolute control and script execution. These two cameras are mounted, individually, on a tripod fitted with a CLAUSS RODEON piXplorer programmable panoramic arm that turns them vertically and horizontally, with an angular resolution of $0,015^\circ$.

For the validation of the 4π method, three additional devices are used to record the weather conditions at the time of the measurement:

- A Testo 405i hot-wire anemometer to measure wind speed and air temperature.
- A thermohygrometer HOBO U12-012 to register the relative humidity and to have a supplementary measurement of the air temperature.
- A black-globe thermometer. This device relates the radiative effect of the scene to the temperature and wind speed for a given globe temperature.

3.2 Imaging pipeline

This section describes the 4π imaging pipeline, which processes thermograms and photographs to produce calibrated radiance maps.

The method is based on the use of passive infrared thermography along with High Dynamic Range (HDR) photography so no additional basic environmental measurements are required. The 4π method is similar for both wavelengths and each step in the pipeline is outlined below.

3.2.1 Image processing. The method seeks to create spherical panoramas (4π imagery); hence, it is imperative to

set up the montage carefully and to determine any distortions that may affect the image assembly. The former prevents the parallax that affects panoramic images due to the movement of the camera. Parallax is the angular deviation of the perceived position of an object relative to the vantage point [Littlefield 2006].

The later helps to identify the exploitable region of the image that is the least affected by distortions. To determine the distortion produced by the lens of the camera, a sequence of images of a calibration standard is captured. For this to work on both devices, it must be performed under the sun. The standard consists of a sheet of paper on which a checkerboard pattern is printed, with alternating black and white squares. Since the sheet of paper has very little inertia, the white color reflects a large part of the light while the black color absorbs it. Therefore, when exposed to the sun, this calibration pattern is immediately observable by the LWIR thermal camera.

The distortion identified for both devices is of positive radial type (known as *barrel distortion*). This type of distortion is often found in wide-angle lenses and is greater at the outer edges of the image. However, image-related artifacts are not exclusively due to the lens. If these artifacts result in a change in the measured radiance of a scene, they can be considered as radiometric artifacts. Typically, an image captured by a camera shows a radial decrease in intensity from the center of the image. This is the so-called *vignetting* effect. In thermography, it affects the image by making the edges appear warmer than they are.

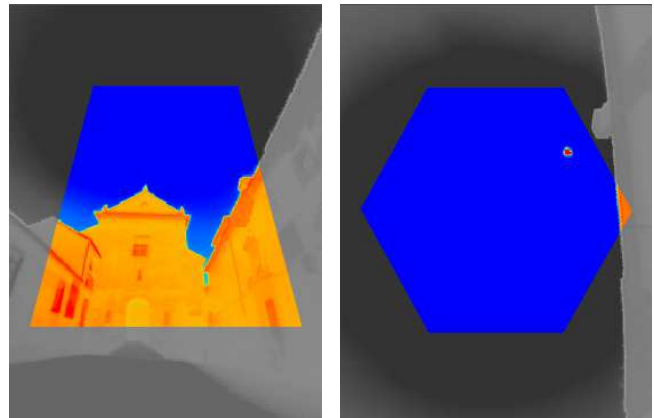


Figure 3. The area used for the assembly of a 4π image at two elevation angles: a) $\pi/6$ rad b) $\pi/2$ rad (zenith image)

Based on this information, the time taken to capture each image and the aperture angle of the lens, it was decided to rotate the camera of $\pi/3$ rad for each capture, thus limiting the area used in each image. This reduces the distortion caused by the lens and the vignetting effect while avoiding any modification that could alter the recorded information measured by the cameras (Figure 3). A complete measurement requires 14 images for each spectrum band and

takes about three minutes. This time is sufficiently short to ignore its effect on the radiant temperature of the scene.

3.2.2 Radiances of the scene. To retrieve the radiances of the scene from the image captured with the LWIR thermal camera, the process is straightforward. Since, by considering that the emissivity of the whole scene is that of a black body and that the atmosphere is perfectly transparent, the image displays equivalent black body temperature, it is possible to calculate the radiance by using equations (2) and (3). These relationships show that the ratio of emittance to the radiance of a Lambertian surface is a factor of π . For such a surface, the emitted energy decreases with the $\cos \theta$, as does the projected surface of the hemisphere when the direction of observation deviates from the normal of the surface. Hence, radiance is defined per unit of the visible surface. For a point in the center of the sphere, this visible surface is the whole sphere, 4π .

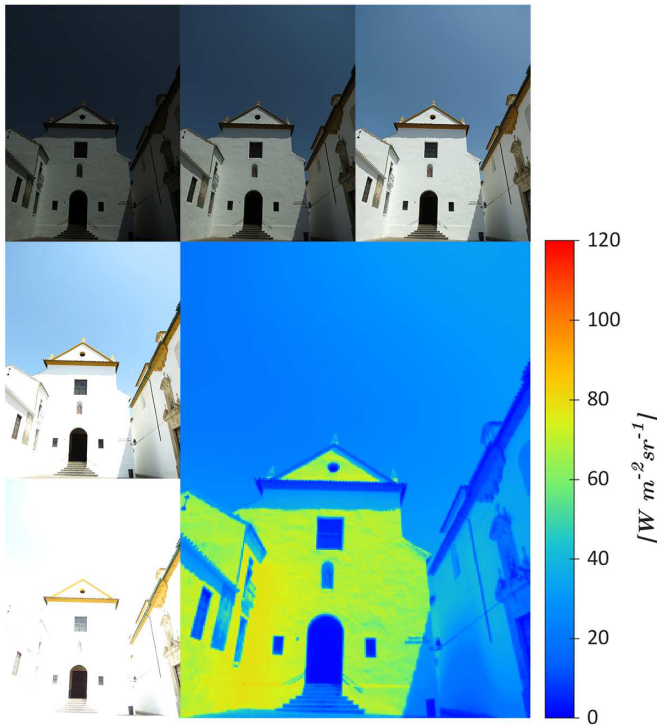


Figure 4. Photographs at several exposures and their corresponding radiance map.

To capture the radiance of the scene in shortwave, High dynamic range (HDR) images are produced by combining several exposures of the same photograph [Debevec 2008]. The capture time is brief, and, consequently, the scene is considered static (Figure 4). The result is evaluated with a luminance meter to ensure correct calibration, then to suppress the correction due to the perception of the luminous flux introduced for human vision, it is necessary to multiply each *RGB* component by its corresponding coefficient [Poynton 2003].

$$L_e = 0.2126 R + 0.7152 G + 0.0722 B \quad (8)$$

Through this process, the energy measured between $7.5 \mu\text{m}$ to $13 \mu\text{m}$ for thermography and $380 \text{ nm} - 780 \text{ nm}$ for photography allows the estimation of the scenes radiances in longwave and in shortwave for the whole spectrum. However, the process is not the same for the sky. It presents some particular features, which require different approaches.

3.2.3 Sky Radiances. The sky is involved in the radiative exchange of most urban scenes. In longwave, its contribution is low. However, its influence is significant and is due to its frequently contrasting low temperature while in shortwave, the sky holds the two main sources of radiation: the sky vault (diffuse) and the sun (direct).

Unlike all other elements of the scene, the sky deserves differentiated treatment in longwave, where it cannot be approximated to a black body.

A calculation of the atmospheric emission using the MODTRAN model [Berk 1989] illustrates the relationship between a clear sky and an overcast sky by comparing both to a black body at air temperature (Figure 5). The spectral radiance of the atmosphere can be seen as a relationship between the radiance of a black body at air temperature and the atmospheric transmittance. As a result, its emissivity is equivalent to that of a black body only when the transmittance is low.

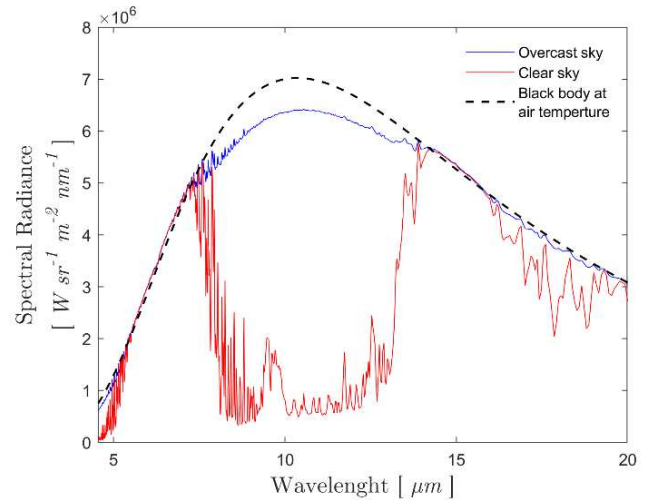


Figure 5. Black body radiance at air temperature 288 K (dashed line) and atmospheric emitted radiance (solid line) for a) Overcast sky ; b) Clear sky.

For a clear sky, this approach results in an underestimation of the sky's radiance which is corrected by adding the integral of the sky's radiance within the atmospheric windows with the integral of a black body's radiance at air temperature for the rest of the spectrum [Kruczek 2015]

In shortwave, the sky is the only source of radiation, and its components (the sky vault and the sun) exhibit very different emission levels. HDR photography extends the range of measurement so that the radiance of the scene and the sky vault can be measured with confidence, not being so for the sun. This is by far the brightest object in the Earth's sky, with orders of magnitude above the sky and clouds, which is much brighter than what cameras are designed to capture.

To overcome this constraint, in the extreme case of a clear sky under direct solar radiation, the measured sky is replaced by a theoretical model of the sky radiation distribution [Perez 1993]. This allows to estimate the contribution of each part of the sky according to the position of the sun.

3.2.4 Projection on the sphere. The hemispherical partition proposed by [Beckers 2012] is adopted in this study and duplicated to build a spherical canvas. This partition offers the possibility for the user to select the number of patches while ensuring that each one maintains the same solid angle and a proper aspect ratio.

In this study, 14 images are assembled in a sphere. 7 of them build a hemisphere, including one that covers the zenith (Figure 6). The value of each patch corresponds to the nearest pixel of the image. The result is a spherical visualization of the scene. In Figure 6, the upper hemisphere is represented in an azimuthal equalent projection [Beckers 2014], which means that the solid angle of an element can be obtained by accounting its pixels.

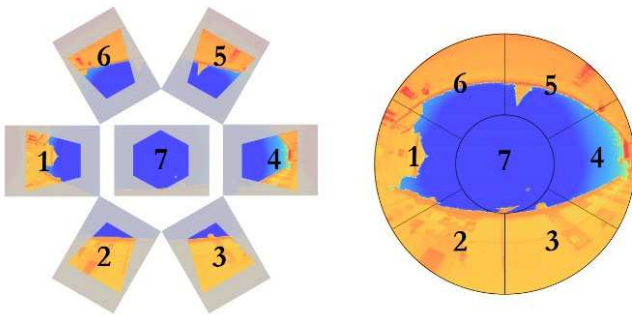


Figure 6. Construction of the hemisphere using 7 thermograms.

3.2.5 Mapping the spherical projection on the plane. The sphere is then projected onto the plane (Figure 7). Other surveys have depicted thermographs using cartographic projections [Asano 1996, Tamura 2001]. To observe and accurately quantify the impact of each surface of the scene, the Mollweide projection is ideal [Beckers 2014, Lapaine 2011]. This is an equivalent projection (relative areas of the sphere are conserved), allowing the solid angle of each surface to be measured directly by accounting the pixels representing it. For the scene of Figure 7, the sky solid

angle [Capeluto 2003] ($SSA = 2.89 \text{ sr} = 0.92 \pi \text{ sr} = 23 \%$ of the sphere area. The concept of the SSA , as it does not depend on a surface or its orientation, applies to any other element of the scene. For instance, for the ground, where it would become *Ground Solid Angle*. The ground solid angle ($GSA = 5.59 \text{ sr} = 1.78 \pi \text{ sr} = 44 \%$ of the sphere area. Finally, the wall solid angle ($WSA = 4.08 \text{ sr} = 1.30 \pi \text{ sr} = 33 \%$ of the sphere area. The sum of these solid angles = $12.56 \text{ sr} = 4 \pi \text{ sr} = 100 \%$ of the sphere area.

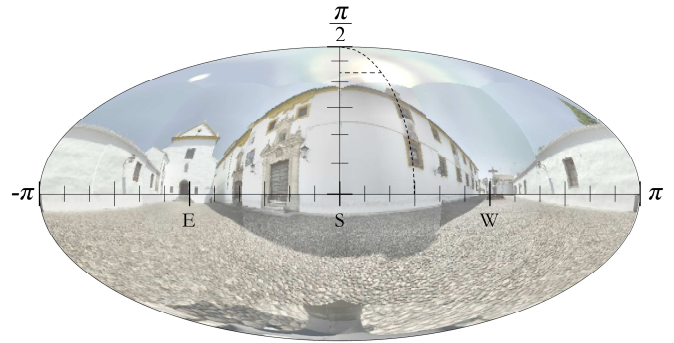


Figure 7. Mollweide projection of Capuchinos Square. (Cordoba - Spain).

To ensure the coherence of the graphics and facilitate comparisons, the scenes are always oriented to the South, so that the centers of the projections always indicate the South in the horizontal reference plane. Both extremities of the horizontal axis indicate the North, they represent the same direction. At mid-distance of the center and the left (right) extremity, we have the East (West) direction.

The Mollweide projection maps on a plane the entire sphere with low distortion everywhere. It displays equidistantly distributed meridians. If we graduate the horizontal axis from $-\pi$ to π , we indicate all the directions from North, East, South, West, and, back to North. The parallels (lines of equal latitude) appear as horizontals (each latitude circle of the sphere contains the projections of all the points with the same zenith angle).

The superposition of the axes allows observing the position of the sun easily. Its azimuthal angle corresponds to the meridian traced in a dashed line and because the Mollweide projection maintains horizontal latitudes, its angle of elevation can be observed simply with respect to the vertical axis. Thus, the vertical axis also marks the solar noon, for the northern hemisphere. At the time of measurement, the sun had an elevation of 66.7° and an azimuth angle of 224.7° .

3.2.6 T_{mrt} calculation with the 4π method. This approach allows measuring the radiances of the entire scene. As the 4π method captures the whole scene around a point, the integration of all radiances L_e [$\text{W m}^{-2} \text{sr}^{-1}$] over the sphere makes it possible to calculate the spherical irradiance

$E_{e,o}$ [W m⁻²] of the scene [CIE 2020] for each part of the spectrum.

$$E_{e,o} = \int_{4\pi} L_e d\Omega \quad (9)$$

By combining both shortwave and longwave spherical irradiances, the total flux is obtained.

$$\phi_r = \alpha_{LW} E_{e,oLW} + \alpha_{sw} E_{e,o_{sw}} \quad (10)$$

Further, since an equivalent partition for the sphere is used, it is possible to obtain the same result directly from the sphere's average, as the total number of cells (N_{patch}) determines the solid angle of each of its cells.

$$\Omega = \frac{N_{patch}}{4\pi} \quad (11)$$

Hence, the T_{mrt} can be calculated as the average flux on the Beckers' sphere.

$$T_{mrt} = \sqrt[4]{\frac{\sum L_e}{N_{patch}}} \quad (12)$$

The 4π method is an alternative to evaluate Mean Radiant Temperature but foremost a tool for visual analysis of the urban radiative environment. Moreover, this method enables certain spectral discrimination. Consequently, it allows studying the environment along three components, time, space, and the spectrum.

4. Result analysis

The next section is divided into two parts. The first compares the results of the 4π method with T_{mrt} measurements from a black-globe thermometer. The second analyses and discusses a selection of graphical results of the 4π method.

4.1 Comparison results

Several case studies were conducted to validate the proposed method. Figure 8 shows 15 different measurements, the first 5 were made during the day in Bayonne (France) the 29 of December, under an overcast sky. The following ones were carried out in Cordoba (Spain) in summer, 5 during the night, and 5 during the day, all of them under a clear sky.

The comparison of the Mean Radiant Temperature obtained from the black-globe ($T_{mrt,g}$, symbol +) and from the imaging method ($T_{mrt,o}$, symbol ○) shows a difference of less than two degrees in all cases.

The lowest temperatures in the table correspond to Bayonne in winter. The small variation between the

temperatures corresponds to stable wind conditions and an overcast sky. For the first measurement inside the cathedral, all the temperatures are very close, thus, representing a highly uniform environment.

The second series shows 5 nocturnal scenes under the clear sky of Cordoba in summer. They all follow the same order: $T_{mrt} < T_g < T_{air}$. This order corresponds to all the measurements made in the absence of solar radiation (shortwaves).

The last series of the table correspond to the same 5 scenes in Cordoba, but at noon. The inversion corresponding to the presence of solar radiation (shortwaves) is immediately observable. Although T_{air} and T_g remain almost equal, T_{mrt} varies in greater magnitude. This difference is related to the *Sky Solid Angle (SSA)* and it can be observed throughout an entire campaign. In the winter series, the temperature ranges for each of the scenes is smaller, even in the presence of a significant sky solid angle. This is due to the cloud cover that significantly changes the temperature of the sky. Therefore, this temperature range is related to the clear sky solid angle.

The comparison between the 4π method and the black-globe method is satisfactory. The method allows T_{mrt} to be determined in a fast and simple way to bypass the influence of convection. The time required for the measurement is of about three minutes, considerably less than with the black-globe thermometer, as there is no need to wait for the sensor to attain the equilibrium.



Figure 8. Comparison of the different temperatures of the scene. The absolute value of $T_{mrt,o} - T_{mrt,g}$ is always inferior to 2 degrees

4.2 Graphical results

The 4π method appears as an alternative to measure T_{mrt} . Its main advantage is to provide a visual representation of the radiative environment for either qualitative or quantitative studies. This depiction uses color maps to represent the radiative distribution of the scene. A simple visual inspection provides a vast amount of qualitative information that can be further refined by adjusting the span and the level. This improves the observer's ability to recognize even small differences in the image due to enhanced contrast.

In photography, *metering* refers to the determination of the optimal exposure for a scene and is done in two different ways: either for the center of the image, as an average, or concerning regions of interest. A similar concept applied to

the 4π method allows metering the radiative scene helping designers, urban planners, to better understand it.

The 4π method proposes a visual metering of the scene, where each element can be easily identified. Thereby, its influence can be precisely quantified.

Inside the Cathedral of Sainte-Marie de Bayonne (Figure 9b), the equivalent black body temperatures are relatively uniform, with differences no greater than 5 degrees (Figure 9c). This is due to the low shortwave radiation and the important inertia of the massive stone structure and walls of the building. Despite this uniformity, it is possible to distinguish that the right side shows a somewhat higher temperature, as it corresponds to the southern façade of the cathedral, which is facing the sun the entire morning as shown by the stereographic diagram (Figure 9a). Low light conditions translate into a minor contribution to shortwaves (Figure 9d). For this scene, this is only of 6.79 W m^{-2} and comes exclusively through the windows. In longwave, the total contribution of this scene is 387.8 W m^{-2} . Even if the highest values of the image correspond to the individual in the room, most of the longwave radiation comes from the cathedral itself (Figure 9e).

This scene complies with the ideal conditions for which the Mean Radiant Temperature was conceived and, through the 4π method it is easy to see why. In such a scene, T_{mrt} depends mostly on longwave radiation and the visualization of the radiative environment reveals that the scene is highly uniform for both longwave and shortwave. This explains why the span needed to represent the two images is reduced; being even more limited for longwave.

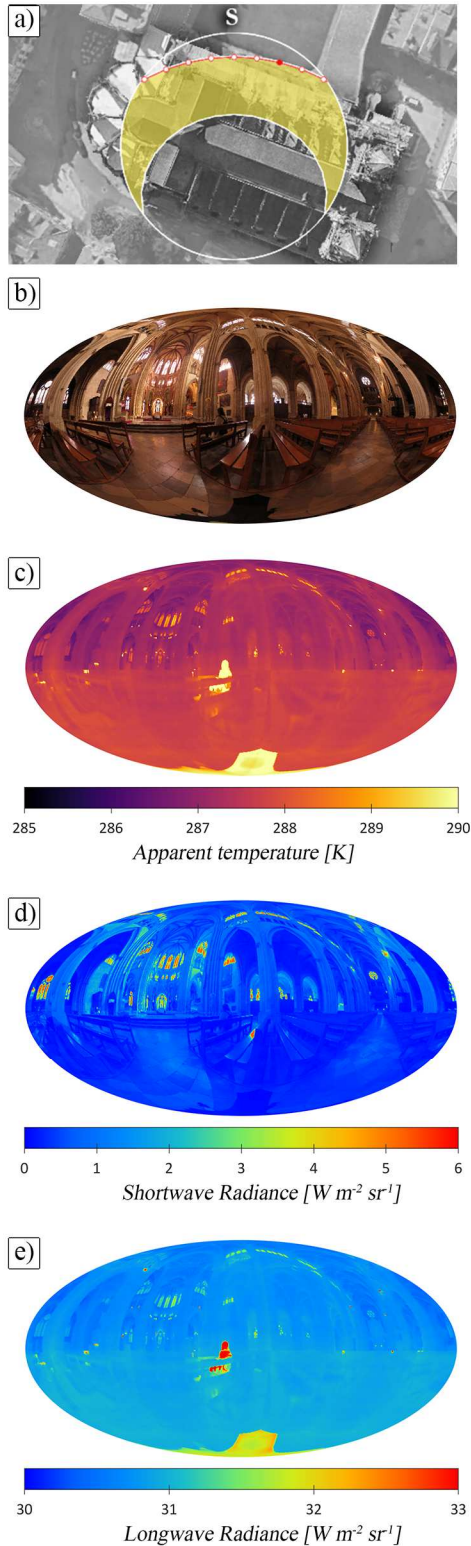


Figure 9. Cathedral of Sainte-Marie (Bayonne – France):
 a) Sunpath b) Photography c) Thermography
 d) Shortwave radiance map e) Longwave radiance map

In Cordoba at Capuchinos Square, the scene is measured twice to observe the variation on radiation fluxes between night and day.

The first measurement is performed during the early morning to completely avoid shortwave contributions. Figure 10 was captured at midnight. In this scene, all temperatures seem very similar, except for the sky, which is much colder.

At night, owing to the absence of shortwave radiation, the color of the surfaces has less influence than their emissivity, which is difficult to determine accurately. A slight difference in emissivity has an impact on the surface temperature. Traditional building materials frequently present similar emissivity above $\varepsilon = 0.90$. Therefore, a subtle dissimilarity in emissivity may explain a temperature difference.

The high emissivity of the elements of an urban scene allows them to be approximated as black body radiators, despite some exceptions. Hence, their emission is always diffuse and the radiative exchanges between elements of the scene are in agreement with their view factors.

The low temperature of the sky contrasts with that of the rest of the scene. Therefore, the surfaces of the scene with a greater view of the sky will exchange more with it. The emission of the scene towards the sky is responsible for the radiative cooling.

However, its influence over the walls and the ground seems not to agree with this. Since the walls' exposition to the sky is lower than that of the ground, the temperature of the walls should be higher. By refining the observation, shortening the span, and increasing the level, this effect can clearly be shown by zooming in on the cobblestone covering the ground of the square. Here, it can be seen how the round stones show a lower temperature in the areas exposed to the sky. In these areas, the temperature is, in fact, lower than the temperature of the walls, while in the interstices it seems to be higher.

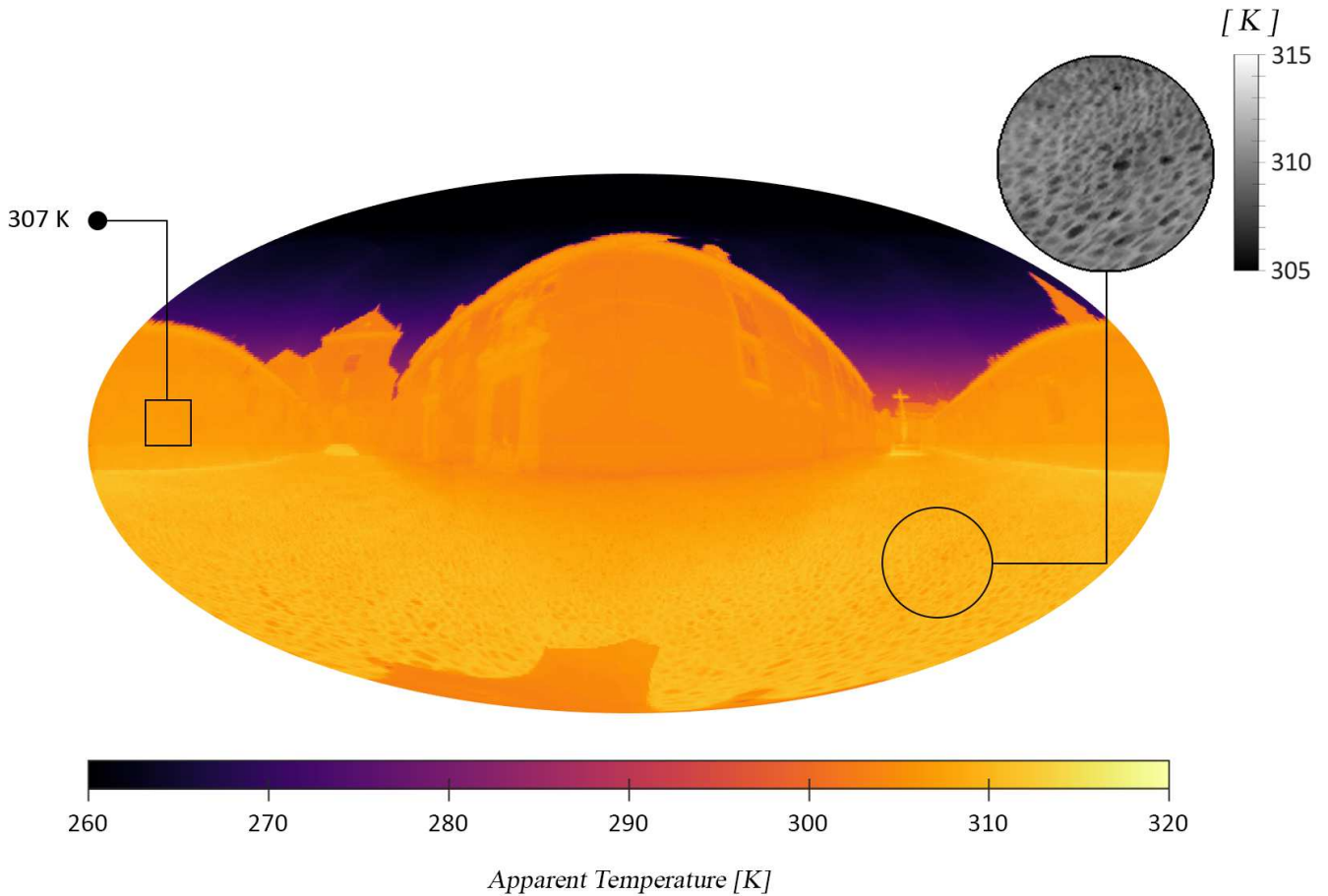


Figure 10. Capuchinos Square (Cordoba – Spain):
Equivalent black body temperature map recorded on July 24th at 00:00 ST

For the same scene, at noon, and under the summer sun, the first difference is the span needed to exploit the image. This measurement was performed an hour and a half after the sun attained its highest point in the sky (Figure 11a) and it was completely cloudless. The values of longwave radiances in Figure 11e are about twice as high as those measured inside the cathedral of Bayonne (Figure 9e). This is due to the high temperatures.

In this scene, three main sources of longwave radiation are easily identified, the sky, the built environment, and the ground. The sky contribution to longwave radiation is the smallest of the scene and diminishes between the horizon and the zenith. The reasons for this are its low temperature, the broader layer of the atmosphere near the horizon, and the absence of clouds.

For shortwaves, the measured radiances (Figure 11d) can be up to ten times higher in Cordoba than in Bayonne as a consequence of the direct solar radiation and the very light colors of the urban façades. During the day, the colors of the

surfaces are of great importance (Figure 11b). Under direct sunlight, the whitewashed masonry walls of the Capuchinos square are the second-largest source of shortwave radiation after the sun. The whitewash coating covering the walls decreases their absorbance α_{sw} within the shortwave spectrum. In Figure 11d, we can see that, when exposed to sunlight, white walls radiate high amounts of energy through reflection ($\rho_{sw} = 1 - \alpha_{sw}$). In contrast, the ground displays much lower values. The grey cobblestone that covers it has a much higher α_{sw} coefficient than the walls. Therefore, it does not reflect as much. Radiation absorbed in shortwave is emitted in longwave. This explains why the wall at the edges of the image, which receives direct sunlight, does not differ much from the wall in the center, which is in shadow. In contrast, since the ground has a much higher α_{sw} coefficient than the walls, it displays much higher longwave values.

For longwave, $E_{e,oLW}$ is equal to 568 W m^{-2} while for shortwave $E_{e,oSW}$ is equal to 394.8 W m^{-2} . As in the other scenes, the longwave irradiance is higher than the shortwave

one but this time the gap is narrower. Although the global contribution is greater in longwave, the local values can become much larger in shortwaves. A visual comparison between Figure 11d and Figure 11e can also reveal some time-related effects of the radiation from a single capture. Shortwave radiation is instantaneous; the wall of the convent interrupts the light, traveling from the sun to the ground of the square. This generates a perfectly delineated shadow. This can be seen in the center of the image. As the sun moves, the shadow moves at the same speed. Longwave radiation behaves differently. It is inertial. As explained before, the square receives energy by shortwave radiation, absorbs it, and then emits it as longwave radiation. Yet, thermal inertia prevents this process from being instantaneous, causing the infrared "shadow" to be blurry.

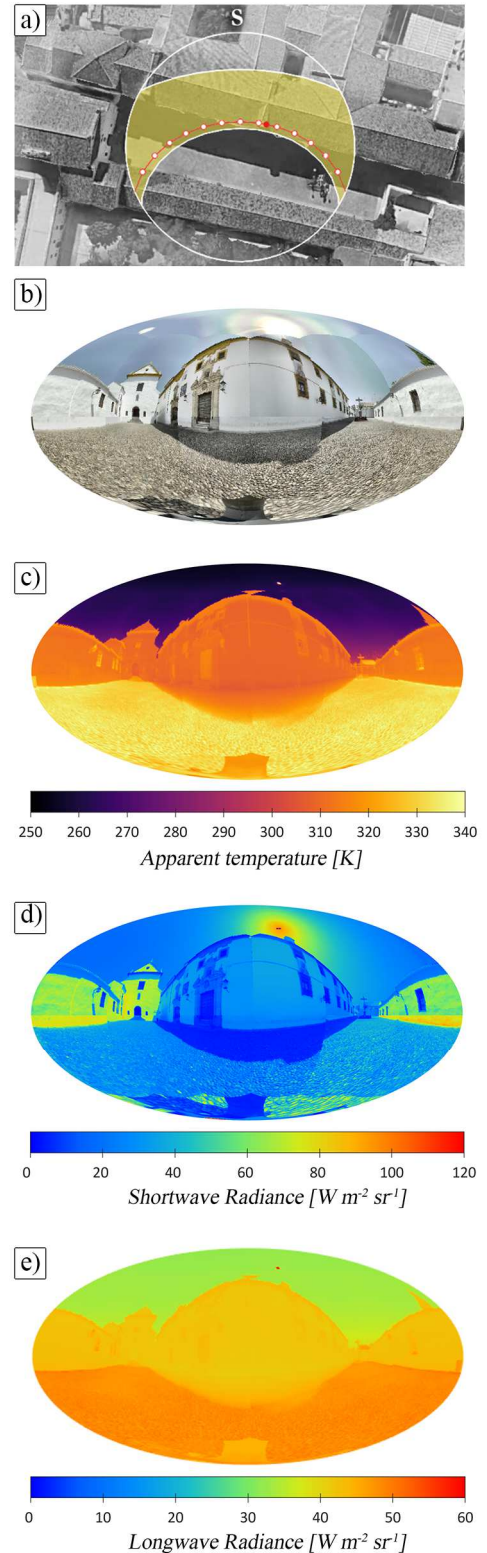


Figure 11. Capuchinos Square (Cordoba – Spain) on July 24th at 13:30 ST
 a) Sunpath b) Photography c) Thermography
 d) Shortwave radiance map e) Longwave radiance map

So far, each part of the spectrum has been studied individually. Combining both in a single graphical representation can have advantages. For a qualitative study, this means improving the information content of the image due to the high detail provided by the shortwaves. This makes it easier to identify the objects or characteristics of the scene, thus, simplifying its interpretation. For a quantitative study, the combination of both images allows the evaluation of the scene in terms of total flux, by determining zones of interest while keeping the link with the geometry of the scene.

This link, which helps to evaluate the radiative scene qualitatively also serves for its geometrical study. Being an equivalent projection, it respects the areas. Hence, the relationship between the sky and the totality of the sphere allows a simple determination of the *Sky Solid Angle (SSA)*.

Bearing in mind that to better understand the radiative environment it is convenient to study it under extreme conditions, it is intended to point out that the scene analyzed in Figures 9-11 was selected because it depicts the earliest morning hour and hottest time of day (13:30 ST) on July 24, 2019. This corresponds to the peak of one of the strongest heat waves in recorded history.

Figure 12 is the result of combining Figure 11d and Figure 11e. This represents the integration of energy within the spectrum while maintaining the spatial component. Therefore, this image (Figure 12) corresponds to the radiative environment that results in a T_{mrt} of 356.4 K. The strong asymmetrical radiant fields that frequently

differentiate an outdoor from an indoor radiant environment are visible.

This scene, which received solar radiation all morning, has now reached its highest temperature even if direct radiation continues to strike the square and its white walls. These walls that reflect the direct radiation from the sun also obstruct the sky and this has a major impact on the radiative balance of the square. Not only does it have a decrease in the outgoing radiation on longwave, but it is also affected by the reflection of shortwave. More importantly, due to the temperature of these surfaces obstructing the sky, the radiative balance has a significant increase in longwave radiation and this is still present at night.

Being able to identify each of the elements of the scene and quantify their influence within the radiative environment can help to prioritize the different possible strategies in an urban project. The first identified element is the sky, which stands out due to its dual character. In longwave, it is responsible for radiative cooling. In shortwave, it is the source of all radiation. Some investigation has been done on strategies to shade the city, by including vegetation, incorporating structures, or textiles [Lee 2018]. Though they all reduce shortwave contributions, they also reduce SSA. The second is the set of vertical surfaces. They represent about a third of the scene and they are responsible for 324 $W m^{-2}$ of the total radiation although almost half of them are in the shade. The third is the ground. In this case, the energy density is lower than that of the walls, but it occupies 90 % of the lower hemisphere.

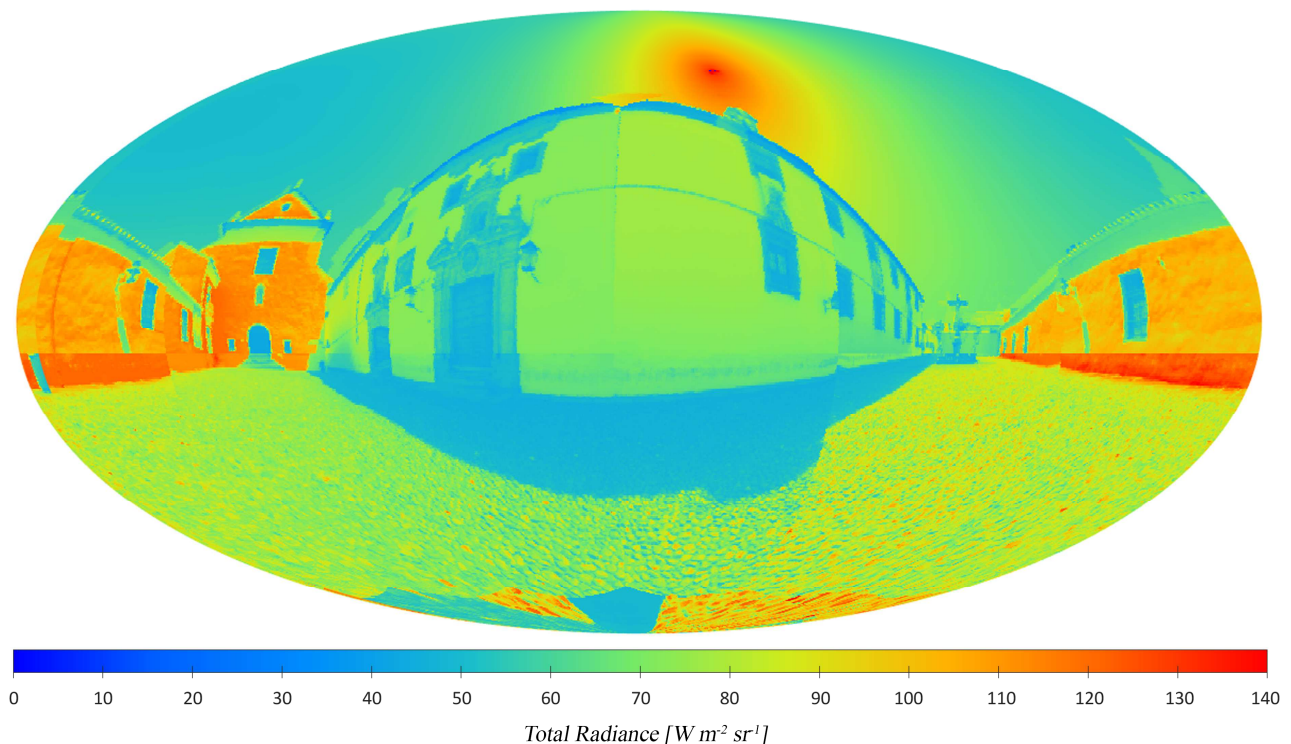


Figure 12. Total radiation map obtained from the combination of shortwave and longwave. Recorded on July 24th at 13:30 ST.

This type of study gathers enough information to guide an urban or architectural project and the ability to visualize the environment allows easy use of the method. The possibility of quantifying radiative and geometric elements of the scene from a single measurement allows the study of urban environments in a precise way. This helps to get a better grasp of the physical phenomenon of radiative exchanges.

5. Discussion

5.1 Contribution to urban physics

The 4π method is a novel approach to estimate the mean radiant temperature. Its visual and geometric result makes it a tool with much more potential than the black globe thermometer. One of its strengths lies in its relationship to the solid angle, which facilitates a better understanding of the urban scene.

To illustrate this idea, the floor of Capuchinos Square (left) is compared to that of the Roman Bridge (right) (Figure 13a). The conditions are similar in both cases and the shortwave irradiance varies only by 2 W m^{-2} . These two stone floors differ exclusively by their texture. The effect of roughness on thermal radiation has been explored theoretically [Sacadura 1972], showing that increased roughness leads to greater emissivity.

Figure 13b and Figure 13c show the longwave radiance of the ground at both locations through equivalent azimuthal projections of the lower hemisphere. Figure 13b shows the two scenes during the day and Figure 13c during the night. Since they were captured from an altitude of 1.2 meters, most of the image is occupied by the ground.

The difference between the two floor textures appears clearly in longwave. A rough surface means a larger exchange area. Although one could expect radiative cooling to be favored, the roughness of the floor retains the heat acquired during the day. Indeed, the geometry of the cobbles leads to only a small surface exchanging with the sky to be cooled while the heat remains trapped between the interstices.

To compare the mean longwave irradiance, a solid angle of 0.52 sr was selected in the center of each scene. This was the biggest solid angle that allowed avoiding the influence of both the urban geometry and the experimental setup. It can be seen that both during daytime (Figure 13b) and nighttime (Figure 13c), a rough textured floor emits more energy than a smooth one. During the day, the difference is of the order of 100 W m^{-2} while at night it is close to 12 W m^{-2} . This represents about 15% less thermal energy emitted by the floor during the hottest hours.

In Capuchinos Square, the ground occupies a solid angle of $1.78 \pi \text{ sr}$, representing the majority (57.14%) of the sphere surface. Replacing the rough floor of the square with a

smooth one that radiates an average of 594.3 W m^{-2} shows that in such a case, a decrease of this extent can represent a drop in the mean radiant temperature of about 3 degrees during the daytime and about 1.5 degrees during the night time. Observations of this nature provide fundamental insights to the urban planner or designer and are only possible through this method, as even through simulation, such a calculation is not possible today.

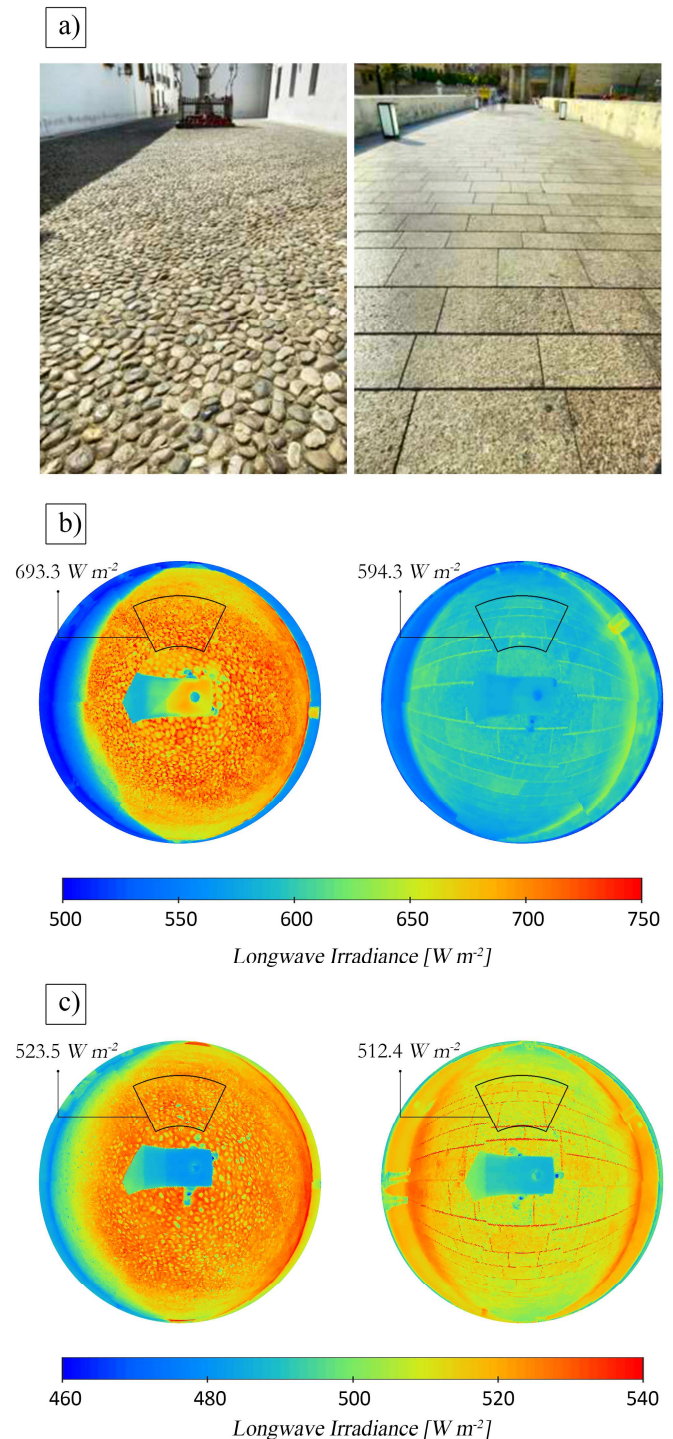


Figure 13. Floor texture. a) Photographic comparison between Capuchinos Square and the Roman Bridge. b) Daytime longwave irradiance c) Nighttime longwave irradiance

5.2 Technical contribution

This method presents a setup that performs well with two standard cameras, albeit on shortwave it is possible to improve the method when the sky is clear and the sun is present. On longwave, the use of a LWIR thermal camera has shown that it is possible to evaluate the scene within its measuring range and extend the result to all longwave.

The LWIR thermal camera has a resolution of 320 x 240 pixels and uses a lens with a field of view of 90° x 73°. In one rotation it captures 1 075 200 pixels. The results showed that only 4 000 pixels are sufficient to calculate the mean radiant temperature. However, for a high visual resolution, 300 000 pixels are recommended. The wide-angle lens reduces the number of images needed to cover the sphere. If the interest leans towards energy performance, the briefness with which measurements can be taken facilitates the capture of time-lapse sequences that allows the evolution of a scene to be observed. However, to deepen the radiative exchanges and the surface temperatures, it is mandatory to project back the spherical image on a 3D model of the scene, which is beyond the scope of this article.

Finally, if time is not a constraint, a cost-effective solution could produce acceptable results with lower specification equipment, even if it requires more images to cover the sphere.

6. Conclusions

The 4π method helps to accurately evaluate the radiative component of an urban scene avoiding the effects of convection. It uses photographic and LWIR thermal cameras. Thus, radiation is measured between 380 nm - 780 nm and 7.5 μ m to 13 μ m and extrapolated to the full shortwave and longwave spectra respectively. The combination of these two measurements yields the total radiance of the scene. As a result, by integrating the results of the 4π method, in the spectrum and space, it is possible to accurately quantify the T_{mrt} in complex environments.

As stated in the introduction, the interest in working on the urban radiative environment is present at different scales. This method has been conceived with the aim of better understanding the radiative phenomenon in the urban scene to be able to act on it. Given the complexity of urban scenes, a measurement capable of synthesizing great amounts of information is helpful and its visual result allows for rapid assessment.

The 4π method is the only way to provide such fundamental insights on the radiative landscape of the city and its strength lies in the relationship of solid angles with the radiometric information of the scene. Other methods of

measurement fall short by not considering the spatial distribution of radiation while, due to the complexity of urban geometry, the required level of detail is not yet reachable for simulation.

References

- [1] Acuña Paz y Miño, J., Lawrence, C. and Beckers, B., 4π Thermography: A projection to Understand Thermal Balance. Proceedings of the 16th IBPSA Conference, Rome, Italy, Sept. 2-4, 2019
- [2] Akbari, H., Cartalis, C., Kolokotsa, D., Muscio, A., Pisello, A.L., Rossi, F., Santamouris, M., Synnefa, A., Wong, N.H. and Zinzi, M., 2016. Local climate change and urban heat island mitigation techniques—the state of the art. *Journal of Civil Engineering and Management*, 22(1), pp.1-16.
- [3] Asano, K., Hoyano, A. and Matsunaga, T., 1996, June. Development of an urban thermal environment measurement system using a new spherical thermography technique. In *Infrared Technology and Applications XXII* (Vol. 2744, pp. 620-631). International Society for Optics and Photonics.
- [4] ASHRAE, Fundamentals Handbook, 2001. SI Edition, American Society of Heating, Refrigeration and Air-Conditioning Engineers, Atlanta, USA.
- [5] Beckers, B. and Beckers, P., 2012. A general rule for disk and hemisphere partition into equal-area cells. *Computational Geometry*, 45(7), pp.275-283.
- [6] Beckers, B., 2013. Worldwide aspects of solar radiation impact. *Solar energy at urban scale*, pp.99-118.
- [7] Beckers, B. and Beckers, P., 2014. *Reconciliation of geometry and perception in radiation physics*. Wiley-ISTE.
- [8] Bedford, T. and Warner, C.G., 1934. The globe thermometer in studies of heating and ventilation. *Epidemiology & Infection*, 34(4), pp.458-473.
- [9] Berk, A., Bernstein, L.S. and Robertson, D.C., 1989. MODTRAN: A Moderate Resolution Model for LOWTRAN 7 (GL-TR-89-0122). *Air Force Geophysics Laboratory, Bedford, Mass.*
- [10] Capeluto, I.G., 2003. The influence of the urban environment on the availability of daylighting in office buildings in Israel. *Building and Environment*, 38(5), pp.745-752.
- [11] Chen, L. and Ng, E., 2012. Outdoor thermal comfort and outdoor activities: A review of research in the past decade. *Cities*, 29(2), pp.118-125.
- [12] CIE - Commission internationale de l'éclairage 2020. *Definition Of Radiance*. [online] Available at: <<http://eivl.cie.co.at/term/1012>> [Accessed on March 2020].
- [13] De Dear, R., 1988. Ping-pong globe thermometers for mean radiant temperatures. *H and V Engineer*, 60(681), pp.10-11.
- [14] Debevec, P.E. and Malik, J., 2008, August. Recovering high dynamic range radiance maps from photographs. In *ACM SIGGRAPH 2008 classes* (p. 31). ACM.
- [15] Erell, E., Pearlmutter, D., Boneh, D. and Kutiel, P.B., 2014. Effect of high-albedo materials on pedestrian heat stress in urban street canyons. *Urban Climate*, 10, pp.367-386.

- [16] Eliasson, I., 1996. Urban nocturnal temperatures, street geometry and land use. *Atmospheric Environment*, 30(3), pp.379-392.
- [17] Fiala, D., Havenith, G., Bröde, P., Kampmann, B. and Jendritzky, G., 2012. UTCI-Fiala multi-node model of human heat transfer and temperature regulation. *International journal of biometeorology*, 56(3), pp.429-441.
- [18] Fanger, P.O., 1972. Thermal comfort, analysis and application in environmental engineering.
- [19] Gagge, A.P., Stolwijk, J.A.J. and Hardy, J.D., 1967. Comfort and thermal sensations and associated physiological responses at various ambient temperatures. *Environmental research*, 1(1), pp.1-20.
- [20] Givoni, B., 1998. *Climate considerations in building and urban design*. John Wiley & Sons.
- [21] Grimmond, C.S.B. and Oke, T.R., 2002. Turbulent heat fluxes in urban areas: Observations and a local-scale urban meteorological parameterization scheme (LUMPS). *Journal of Applied Meteorology*, 41(7), pp.792-810.
- [22] Höppe, P., 1999. The physiological equivalent temperature—a universal index for the biometeorological assessment of the thermal environment. *International journal of Biometeorology*, 43(2), pp.71-75.
- [23] Kántor, N. and Unger, J., 2011. The most problematic variable in the course of human-biometeorological comfort assessment—the mean radiant temperature. *Open Geosciences*, 3(1), pp.90-100.
- [24] Koch, W., 1961. A Method of Calibrating Two-Sphere Non-directional Radiometers. *Nature*, 192(4806), p.960.
- [25] Lapaine, M., 2011. Mollweide Map Projection. *KoG*, 15(15.), pp.7-16.
- [26] Lee, I., Voogt, J.A. and Gillespie, T.J., 2018. Analysis and comparison of shading strategies to increase human thermal comfort in urban areas. *Atmosphere*, 9(3), p.91.
- [27] Lindberg, F., Holmer, B. and Thorsson, S., 2008. SOLWEIG 1.0—Modelling spatial variations of 3D radiant fluxes and mean radiant temperature in complex urban settings. *International journal of biometeorology*, 52(7), pp.697-713.
- [28] Lindberg, F., Grimmond, C.S.B., Gabey, A., Huang, B., Kent, C.W., Sun, T., Theeuwes, N.E., Järvi, L., Ward, H.C., Capel-Timms, I. and Chang, Y., 2018. Urban Multi-scale Environmental Predictor (UMEP): An integrated tool for city-based climate services. *Environmental modelling & software*, 99, pp.70-87.
- [29] Littlefield, R., 2006. Theory of the “No-Parallax” Point in Panorama Photography. [online] Available at: <<http://www.janrik.net/PanoPostings/NoParallaxPoint/TheoryOfTheNoParallaxPoint.pdf>> [Accessed on September 2018].
- [30] Martin, M. and Berdahl, P., 1984. Summary of results for the spectral and angular sky radiation measurement program. *Solar Energy*, 33(3), pp.241-252.
- [31] Nikolopoulou, M. and Lykoudis, S., 2007. Use of outdoor spaces and microclimate in a Mediterranean urban area. *Building and environment*, 42(10), pp.3691-3707.
- [32] Oke, T.R., 1982. The energetic basis of the urban heat island. *Quarterly Journal of the Royal Meteorological Society*, 108(455), pp.1-24.
- [33] Oke, T.R. and Cleugh, H.A., 1987. Urban heat storage derived as energy balance residuals. *Boundary-Layer Meteorology*, 39(3), pp.233-245.
- [34] Pearlmutter, D., Berliner, P. and Shaviv, E., 2006. Physical modeling of pedestrian energy exchange within the urban canopy. *Building and environment*, 41(6), pp.783-795.
- [35] Perez, R., Seals, R. and Michalsky, J., 1993. All-weather model for sky luminance distribution—preliminary configuration and validation. *Solar energy*, 50(3), pp.235-245.
- [36] Poynton, C., 2003. Digital video and HDTV algorithms and interfaces. *Morgan Kaufmann Publishers, San Francisco*, 260, p.292.
- [37] Ren, C., Ng, E.Y.Y. and Katzschner, L., 2011. Urban climatic map studies: a review. *International journal of climatology*, 31(15), pp.2213-2233.
- [38] Richards, C.H., Stoll, A.M. and Hardy, J.D., 1951. The panradiometer: An absolute measuring instrument for environmental radiation. *Review of Scientific Instruments*, 22(12), pp.925-934.
- [39] Sacadura, J.O., 1972. Influence de la rugosité sur le rayonnement thermique émis par les surfaces opaques: Essai de modèle. *International Journal of Heat and Mass Transfer*, 15(8), pp.1451-1465.
- [40] Santamouris, M., Papanikolaou, N., Livada, I., Koronakis, I., Georgakis, C., Argiriou, A. and Assimakopoulos, D.N., 2001. On the impact of urban climate on the energy consumption of buildings. *Solar energy*, 70(3), pp.201-216.
- [41] Santamouris, M., 2014. Cooling the cities—a review of reflective and green roof mitigation technologies to fight heat island and improve comfort in urban environments. *Solar energy*, 103, pp.682-703.
- [42] Takebayashi, H. and Moriyama, M., 2007. Surface heat budget on green roof and high reflection roof for mitigation of urban heat island. *Building and environment*, 42(8), pp.2971-2979.
- [43] Tamura, T., Hoyano, A., Aoki, H. and Asano, K., 2001, March. Developing the capturing system of spherical thermograph and applications to built environment. In *Thermosense XXIII* (Vol. 4360, pp. 169-176). International Society for Optics and Photonics.
- [44] Thorsson, S., Lindberg, F., Eliasson, I. and Holmer, B., 2007. Different methods for estimating the mean radiant temperature in an outdoor urban setting. *International Journal of Climatology: A Journal of the Royal Meteorological Society*, 27(14), pp.1983-1993.
- [45] Vernon, H.M., 1932. The measurement of radiant heat in relation to human comfort. *Journal of Industrial Hygiene*, 14, pp.95-111.
- [46] Voogt, J. 2002. *Urban Heat Island*. In Munn, T. (ed.) *Encyclopedia of Global Environmental Change, Vol. 3*. Chichester: John Wiley and Sons.